TUDelft

Delft University of Technology

Additively manufactured metallic porous biomaterials based on minimal surfaces
A unique combination of topological, mechanical, and mass transport properties

Bobbert, Francoise; Lietaert, K.; Eftekhari, A.A.; Pouran, Behdad; Ahmadi, Mohammad; Weinans, Harrie; Zadpoor, Amir

Important note
To cite this publication, please use the final published version (if applicable).
Please check the document version above.

Full length article

Additively manufactured metallic porous biomaterials based on minimal surfaces: A unique combination of topological, mechanical, and mass transport properties

F.S.L. Bobbert [a,*], K. Lietaert [b,c], A.A. Eftekhari [d], B. Pouran [a,e], S.M. Ahmadi [a], H. Weinans [a,e], A.A. Zadpoor [a]

[a] Department of Biomechanical Engineering, Delft University of Technology, Mekelweg 2, Delft 2628CD, The Netherlands
[b] 3D Systems–LayerWise NV, Grauwmeer 14, 3001 Leuven, Belgium
[c] Department of Materials Engineering, KU Leuven, Kasteelpark Arenberg 44, 3001 Leuven, Belgium
[d] Danish Hydrocarbon Research & Technology Centre, Technical University of Denmark, Electrovej Building 375, 2800 Lyngby, Denmark
[e] Department of Orthopedics and Department of Rheumatology, University Medical Center Utrecht, Heidelberglaan100, 3584CX Utrecht, The Netherlands

ABSTRACT

Porous biomaterials that simultaneously mimic the topological, mechanical, and mass transport properties of bone are in great demand but are rarely found in the literature. In this study, we rationally designed and additively manufactured (AM) porous metallic biomaterials based on four different types of triply periodic minimal surfaces (TPMS) that mimic the properties of bone to an unprecedented level of multi-physics detail. Sixteen different types of porous biomaterials were rationally designed and fabricated using selective laser melting (SLM) from a titanium alloy (Ti-6Al-4V). The topology, quasi-static mechanical properties, fatigue resistance, and permeability of the developed biomaterials were then characterized. In terms of topology, the biomaterials resembled the morphological properties of trabecular bone including mean surface curvatures close to zero. The biomaterials showed a favorable but rare combination of relatively low elastic properties in the range of those observed for trabecular bone and high yield strengths exceeding those reported for cortical bone. This combination allows for simultaneously avoiding stress shielding, while providing ample mechanical support for bone tissue regeneration and osseointegration. Furthermore, as opposed to other AM porous biomaterials developed to date for which the fatigue endurance limit has been found to be ≈20% of their yield (or plateau) stress, some of the biomaterials developed in the current study show extremely high fatigue resistance with endurance limits up to 60% of their yield stress. It was also found that the permeability values measured for the developed biomaterials were in the range of values reported for trabecular bone. In summary, the developed porous metallic biomaterials based on TPMS mimic the topological, mechanical, and physical properties of trabecular bone to a great degree. These properties make them potential candidates to be applied as parts of orthopedic implants and/or as bone-substituting biomaterials.

Statement of Significance

Bone-substituting biomaterials aim to mimic bone properties. Although mimicking some of bone properties is feasible, biomaterials that could simultaneously mimic all or most of the relevant bone properties are rare. We used rational design and additive manufacturing to develop porous metallic biomaterials that exhibit an interesting combination of topological, mechanical, and mass transport properties. The topology of the developed biomaterials resembles that of trabecular bone including a mean curvature close to zero. Moreover, the developed biomaterials show an unusual combination of low elastic modulus to avoid stress shielding and high strength to provide mechanical support. The fatigue resistance of the developed biomaterials is also exceptionally high, while their permeability is in the range of values reported for bone.

* Corresponding author.
  E-mail address: f.s.l.bobbert@tudelft.nl (F.S.L. Bobbert).

1. Introduction

Porous biomaterials that mimic the various properties of bone are in great demand. That is due to their utility in substituting bone and their application in various types of orthopedic implants that need to avoid stress shielding while offering enough mechanical support and long fatigue life. Moreover, the mass transport properties of bone-mimicking porous biomaterials such as their permeability have to be properly designed [1–3] to allow for nutrition and oxygenation of cells residing in the inner space of the porous biomaterials. Fully porous biomaterials provide multiple advantages as compared to other types of biomaterials [4]. These advantages include greater flexibility in adjustment of mechanical properties [5], increased surface area that could be used for biofunctionalization and infection prevention [6], and a large pore space that facilitates bone ingrowth and drug delivery from within the implants [7].

Design and manufacturing of porous biomaterials that simultaneously satisfy all the above-mentioned criteria in terms of mechanical and mass transport properties, are challenging enough but not necessarily sufficient for the desired level of bone tissue regeneration. Geometry in general, and the curvature of the surface on which cells reside in particular, has recently emerged as an important factor that determines the rate of tissue regeneration [8]. Multiple studies have, for example, shown that tissue regeneration increases with curvature and that tissue regeneration progresses much further on concave surfaces as compared to convex and flat surfaces [8–11]. Design and manufacturing of porous biomaterials whose curvature is most favorable for bone tissue regeneration have therefore received increasing attention to improve bone tissue regeneration. This coincides with recent advances in the additive manufacturing techniques. These advances enable the fabrication of tissue engineering porous biomaterials with arbitrarily complex geometries for an ever-expanding portfolio of biomaterials.

Minimal surfaces are mathematically rigorous concepts from the differential geometry of surfaces (Fig. 1). In non-mathematical terms, minimal surfaces are like soap films. These films span a minimal surface area between given boundaries [12]. The specific property that makes minimal surfaces appealing for bone tissue regeneration is that they have a mean curvature of zero. A mean curvature of zero, as noted by others [13], resembles the mean curvature of trabecular bone, which is also known to be close to zero [14,15]. Moreover, minimal surfaces are frequently found in nature and tissues of a variety of species [16,17]. Examples, as nicely summarized by Kapfer et al. [17], include "beetle shells, weevils, butterfly wingscales and crustacean skeletons" [18–22]. It has been recently hypothesized that porous biomaterials based on minimal surfaces demonstrate enhanced bone tissue regeneration performance [8].

In the present study, we aimed to generate porous biomaterials based on triply periodic minimal surfaces (TPMS) (minimal surfaces with "translational symmetries in three independent directions" [12]) that present a unique combinations of topological, mechanical, and mass transport properties. With these properties they mimic the various properties of bone to an unprecedented level of multi-physics detail. Rational design and additive manufacturing were used to generate these biomaterials. The 'rational' design of biomaterials refers to the process of utilizing physical/biological principles and the established relationships between the topology of biomaterials and their performance to devise certain 'design criteria'. It is assumed that simultaneous satisfaction of relevant design criteria will result in improved bone tissue regeneration performance. The design process started from four different types of TPMSs and took a number of other design condensations into account to produce a large set of variations of porous biomaterials with different dimensions, porosities, and unit cell types. We used selective laser melting (SLM) for production of metallic porous biomaterials at the micro-scale. SLM is an additive manufacturing process in which successive addition of layers based on a computer-aided design (CAD) is used for free-form fabrication of three-dimensional metal parts. The biomaterials fabricated using SLM have precisely-controlled and highly reproducible micro-architectures. Both of those features are essential for realizing the advantages of rationally designed geometries. We studied the topological, quasi-static mechanical properties, fatigue resistance, and permeability of all types of the designed and additively manufactured porous biomaterials to evaluate their success in mimicking the various properties of bone.

2. Materials and methods

2.1. Porous biomaterial design and manufacturing

Four TPMS structures, primitive (P), I-WP (I), gyroid (G), and diamond (D) were generated using *k3DSurf*, a software which provides all the options to produce complex 3D geometries in a finite volume with the use of implicit functions and inequalities. Because
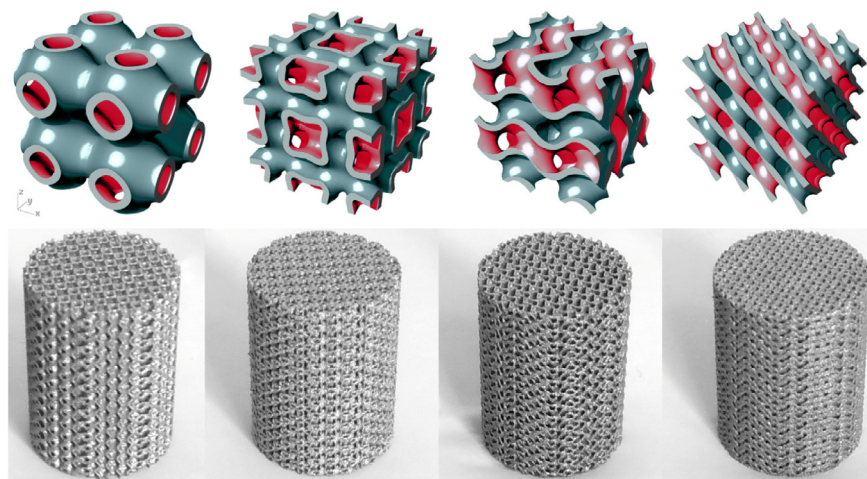
Fig. 1. TPMS porous biomaterials. Top: STL file assemblies of 1.5 mm unit cells, bottom: cylindrical specimens with a height of 20 mm and a diameter of 15 mm manufactured with selective laser melting. From left to right: primitive, I-WP, gyroid, diamond.

the only available file export option in K3Dsurf is .OBJ, a CAD converter software (*MeshLab*) was used to convert OBJ files to STL file format. Finally, STL files were imported to ABAQUS/CAE 6.13 [23]. By keeping the size of the unit cell constant (1.5 × 1.5 × 1.5 mm) and varying the sheet thickness of the TPMSs, four porosities between 43% and 77% per minimal surface type were designed. The porous biomaterials with the highest porosity to the lowest porosity are indicated by the numbers 500, 600, 700 or 800 that follow after P, I, G or D. For example, the P500 has the highest porosity of the primitive porous biomaterials and the P800 the lowest porosity. Magics (Materialise, Belgium) was used to assemble the porous biomaterials based on the different TPMS unit cells. The open porous titanium (Ti6Al4V Grade 23 ELI) biomaterials were built on support structures with a customized version of the 3D Systems ProX DMP 320 machine at LayerWise N.V. (Belgium). Cylindrical specimens with a designed height of 20 mm and a diameter of 15 mm were produced (Fig. 1). The details of the manufacturing process can be found in the supplementary document accompanying the paper.

2.2. Porous biomaterial morphology

The morphology of the porous biomaterials was characterized using micro-computed tomography (micro-CT) and the dry weighing method. Four samples of every type of porous biomaterial were scanned using a micro-CT scanner (Quantum FX, Perkin Elmer, USA).

A tube voltage of 90 kV, tube current of 180 μA, a scan time of 3 min, and a voxel size of 60 × 60 × 60 μm^3 were used. This resolution was used because our micro-CT scanner has a field of view (FOV)-dependent spatial resolution. Therefore, it would not be possible to scan the whole porous biomaterials of 20 mm in length with higher resolutions, e.g. voxel size of 20 × 20 × 20 μm^3. If we used a higher resolution, the calculations would not be representative of the entire geometry. Furthermore, a voxel size of 60 × 60 × 60 μm^3 should be sufficient to capture the details of trabecular thickness and spacing as well as porosity.

The projection images were reconstructed using built-in software of the scanner, and transferred to Analyze 11.0 software to obtain 2D slices, representing the cross-sections of the specimens. Fiji *v.1.49s* [24] in combination with the plugin BoneJ *v.1.4.0* [25] was used for the segmentation of the images. First, the lower limit for the brightness level was adjusted to make sure only the Ti-6Al-4V was visible in the slices. Then the auto local threshold was applied, which computes the threshold value for each voxel within a specified radius in an 8-bit image. The Bernsen algorithm was selected with a radius of 6. This combination was chosen, because it gave the best results for the segmentation of the data when all algorithms available were evaluated by observation. After segmentation, circular regions of interests (ROIs) were created on the cross section of the specimens. The Fiji plugin BoneJ *v.1.4.0* [25] was then used to three-dimensionally compute the morphological properties of the porous biomaterials. The porosity of porous biomaterials was determined using the "volume fraction" option, the pore size (Tb.Sp) and sheet thickness (Tb.Th) were retrieved with the "thickness" option. The surface area was obtained with "isosurface" option using a resampling value of 3 and a threshold of 128, and the degree of anisotropy (DA) was determined with the default settings of the "anisotropy" option with a value of 20 for the minimum amount of spheres and a tolerance of 0.0005.

The dry weighing method is based on the assumption that Ti-6Al-4V has a specific density of 4.51 g/cc. By weighing the specimen and dividing this mass by the mass of a solid cylinder with the same outer dimensions, the material percentage or apparent density (AD) of the specimen was determined. The porosity φ was defined as $\varphi = 1 - AD$.

2.3. Permeability

The permeability of the porous biomaterials was determined using experiments. Eq. (1) (Darcy's law) and Eq. (2) were used to determine the permeability and the Reynolds number (Re), respectively. The Reynolds number indicates whether the flow is laminar or turbulent. For porous media, the flow was assumed to be laminar if 1 < Re < 10 [26]. The micro-CT data for the pore size was used as the pore diameter *d* (Table 2) to determine the Reynolds number (Eq. (2)).

$$\kappa = \frac{v \cdot \mu \cdot L}{\Delta P} \tag{1}$$

and

$$Re = \frac{v \cdot \rho \cdot d}{\mu} \tag{2}$$

where

    κ Permeability coefficient [m^2]
    μ Dynamic viscosity coefficient of the fluid [Pa·s]
    L Height of the sample [m]
    v Darcy (superficial) velocity [m/s]
  ΔP Pressure difference [Pa]
  Re Reynolds number [–]
    ρ Density of the fluid [kg/m^3]
    d Diameter of the pore [m]

2.3.1. Permeability measurements

The falling head method was used in the permeability experiments. In this method, a column above the sample provides the water head. A vacuum pump was used to fill this column with water. When the column was filled, the air valve was opened and the water flowed back into the tank through the sample (Fig. 2). The samples were wrapped with heat shrink tubing and then pressed into a rubber holder to ensure a tight fit and prevent leakage from the sides.

The water pressure at the bottom of the column was measured just above the porous biomaterial with a pressure gauge and registered every second in LabView (v.11.0).

Four samples of every type of porous biomaterial were used in the permeability experiments. The process described above was repeated five times for every sample, resulting in twenty measurements for every specimen. Six steps were taken to derive the permeability from the experimental results.

1. The difference in water level per second within the water column was used to determine the fluid velocity within the column $v_{column} = \frac{\partial h}{\partial t}$, where h is calculated from the measured pressure using Eq. (4b).
2. The volumetric flow rate was computed by multiplying this velocity by the cross-sectional area of the column (A_{column}), perpendicular to the flow direction.
3. The volumetric flow rate (Q) was divided by the cross-sectional area of the specimen ($A_{biomaterial}$) to derive the flow velocity through the sample.
4. In the graph where the pressure drop ΔP (Eq. (4)) was plotted as a function of the velocity of the fluid through the specimen ($v_{biomaterial}$), a power law ($R^2 > 0.998$) was fitted to the data. This power law was then used to extrapolate the data for velocities close to 0.
5. The Reynolds number was computed using Eq. (2), where v is defined in Eq. (3).
6. In the region where the Reynolds number was between Re = 1 and Re = 10, which is the laminar regime in porous media, Darcy's law could be applied [26]. For all specimens, the slope in this region was computed. As described in Darcy's law, this
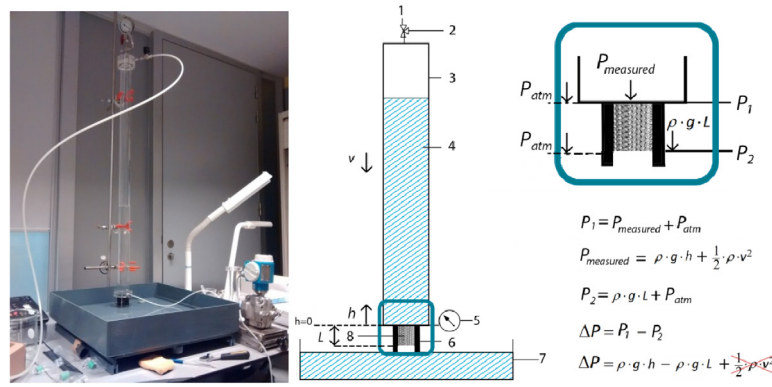
Fig. 2. Permeability experiment set-up. Left: picture. Center: schematic overview 1. vacuum pump, 2. air valve, 3. water column, 4. water, 5. pressure gauge, 6. sample holder, 7. water container, 8. sample. Right: pressure difference over the sample [Pa], with h – water level within the column [m], L – length of the sample, ρ – density of the water [kg/m^3], g – gravitational acceleration [m/s^2], P_{atm} – atmospheric pressure [Pa], v – fluid velocity within the water column [m/s]. The kinetic terms $(1/2 \cdot \rho \cdot v^2)$ is negligible, because this term is relatively small compared to the pressure applied by the water $(\rho \cdot g \cdot h)$.

slope is equal to the reciprocal of the permeability κ, multiplied by the dynamic viscosity coefficient (μ) and the length of the specimen (L), i.e. $\frac{\mu \cdot L}{\kappa}$.

The steps described are summarized in Darcy's law (Eq. (1)), where v and ΔP are defined as

$$v = v_{biomaterial} = \frac{v_{column} \cdot A_{column}}{A_{biomaterial}} \tag{3}$$

and

$$\Delta P = P_{measured} - \rho \cdot g \cdot L \tag{4}$$

where

$v_{biomaterial}$	Fluid velocity through the specimen [m/s]
v_{column}	Fluid velocity within the column [m/s]
A_{column}	Cross sectional area of the column [m^2]
$A_{biomaterial}$	Cross sectional area of the specimen [m^2]
h	Water level within the column [m]

Because the kinetic term $(\frac{1}{2} \cdot \rho \cdot v^2)$ in $P_{measured} = \rho \cdot g \cdot h + \frac{1}{2} \cdot \rho \cdot v^2$ was relatively low compared to the pressure of the water within the column, this term was neglected. Hence, $P_{measured} = \rho \cdot g \cdot h$ (4b). The values for the used parameters are summarized in Table 1.

2.4. Mechanical testing

Nine samples of every type of porous biomaterial were used for the mechanical tests. Six samples were subjected to static compression, i.e. three with and three without lubrication. Another three samples were used for compression-compression fatigue tests.

Table 1
Parameters and their values used in Darcy's law and the equation for the Reynolds number for the permeability experiments.

Symbol	Parameter	Value	SI Unit
ρ	Density of water	10^3	[kg/m^3]
μ	Dynamic viscosity coefficient of water	10^{-3}	[Pa·s]
L	Length of the specimen	20×10^{-3}	[m]
A_{column}	Cross sectional area of the column	1.26×10^{-3}	[m^2]
$A_{biomaterial}$	Cross sectional area of the specimen	1.77×10^{-4}	[m^2]
g	Gravitational acceleration	9.81	[m/s^2]

2.4.1. Static mechanical testing

The static mechanical tests were carried out using an Instron 5500R mechanical testing machine with a 100kN load cell and Bluehill v3.61 software to control the machine and record the measurements. According to the standard for compression of porous and cellular metals (ISO 13314 [27]), a constant deformation rate of 10^{-2}/s should be applied to the samples. This corresponds to 1.2 mm/min for all samples with a height of 20 mm. The sample was placed between two flat hard metal machine platens and only vertical movement was allowed. When the limit of 99 kN, or a displacement of 16 mm was reached, the test was terminated. The strain was measured by the displacement of the crossheads. As described in ISO 13314 [27], the plateau stress (σ_{pl}) was determined as the arithmetical mean of the stresses between 20% and 30% compressive strain. The quasi-elastic gradient was determined by the slope between the strains and stresses within the elastic region of the stress-strain curve. The yield stress (σ_y) was found by the intersection of the stress-strain curve and a line parallel to the quasi-elastic gradient line at a strain offset of 0.2%. During the static mechanical tests, barrelling was observed in some samples. Barrelling is a defect caused by friction at the interface of the machine platens and the end surfaces of the specimen, and causes the sample to become barrel-shaped. To determine if this defect could be reduced by reducing the friction at the interface, tests with and without molybdenum disulfide (MoS$_2$) lubricant at the interface of the platens and the end surfaces of the specimen were performed.

2.4.2. Fatigue mechanical tests

A Materials Test System (MTS) testing machine was used for compression-compression fatigue experiments. Three samples of every type of porous biomaterial were tested at a constant force ratio R = 0.1 ($R = F_{min}/F_{max}$, where F_{min} and F_{max} are the applied minimum and maximum forces, respectively [28]) using a sinusoidal waveform at a frequency of 15 Hz. The maximum force (F_{max}) applied during the fatigue tests was equal to 60% of the yield stress (σ_y). This value was derived from the static mechanical tests without lubricant. The test was terminated when the sample was fractured or when 10^6 cycles were reached without macroscopic failure of the specimen. When the deviation from the mean amount of cycles to failure was higher than 40% between the samples tested for a single load level, a fourth sample was tested. To see the cracks within the specimens after fatigue testing, one sample of every TPMS geometry was embedded. The embedded samples were ground with P320, P800 and P1200 SiC paper, polished

Table 2
Morphological parameters of the different types of porous biomaterials.

	Porosity φ [%]				Sheet thickness [μm] (Tb.Th)					Pore size [μm] (Tb.Sp)		Surface area [μm²]		DA	
	Design	Dry weight	Micro-CT	SD	Design	Micro-CT from top	SD	Micro CT from side	SD	Micro-CT	SD	Micro-CT	SD	Micro-CT	SD
P500	77	71	71	0.59	216	244	33	246	30	896	240	1.26E+10	1.25E+08	0.36	0.01
P600	62	60	61	0.67	294	320	39	321	37	823	237	1.12E+10	5.46E+07	0.29	0.02
P700	56	55	56	0.81	333	349	39	351	36	791	244	1.07E+10	3.98E+07	0.27	0.03
P800	50	49	50	0.29	381	398	43	400	41	722	244	1.03E+10	5.37E+07	0.20	0.01
I500	65	65	54	0.50	155	271	41	275	38	392	99	1.72E+10	3.52E+08	0.13	0.01
I600	57	56	49	1.16	196	298	49	304	47	390	121	1.58E+10	5.20E+08	0.20	0.03
I700	52	52	45	1.28	221	326	56	330	53	383	126	1.43E+10	3.79E+08	0.17	0.04
I800	44	44	39	0.42	250	362	64	367	62	361	130	1.29E+10	4.50E+08	0.18	0.04
G500	69	66	62	0.93	169	258	41	261	39	464	72	1.62E+10	1.12E+08	0.25	0.09
G600	63	62	58	0.74	178	272	38	272	37	458	76	1.58E+10	1.72E+08	0.30	0.01
G700	57	58	54	1.20	230	295	39	296	38	435	75	1.47E+10	2.77E+08	0.26	0.02
G800	51	52	48	0.80	261	330	41	332	40	406	76	1.38E+10	1.41E+08	0.24	0.00
D500	61	60	47	0.52	163	292	37	291	38	370	58	1.82E+10	1.13E+08	0.30	0.01
D600	57	52	41	1.85	196	375	66	370	67	429	99	1.12E+10	3.42E+08	0.26	0.01
D700	49	48	37	0.9	203	430	63	428	66	427	99	1.06E+10	3.75E+08	0.26	0.02
D800	43	44	35	0.33	247	444	61	442	66	413	98	1.01E+10	1.81E+08	0.21	0.01

Tb.Th., trabecular thickness, Tb. Sp., trabecular spacing, DA, degree of anisotropy.
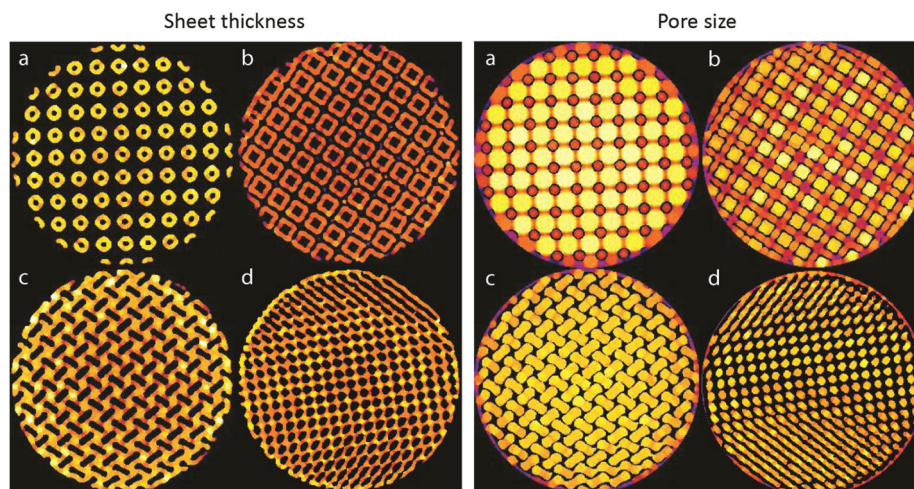
Fig. 3. Micro-CT images of the sheet thickness and pore size. Sheet thickness: maximal spheres fitted into sheets. Pore size: maximal spheres fitted into pores. a. P500, b. I-WP500, c. G500, d. D500.

with 3 μm diamond suspension, and observed using an Olympus BX60M light optical microscope (LOM).

3. Results

### 3.1. Morphology of the porous biomaterials

For every unit cell, the porosity decreases with increasing sheet thickness and the surface area decreases with decreasing porosity (Table 2). The porosities measured with the dry weighing method lay between 71–49%, 65–44%, 66–52% and 60–44% for the primitive, I-WP, gyroid and diamond porous biomaterials, respectively. These values are comparable to the porosities of the design porosity and the values retrieved from the micro-CT scans (Table 2). A lower surface area was observed for the primitive and diamond specimens compared to the I-WP and gyroid specimens. During the analysis of the micro-CT images, spheres with a maximum size were fitted into the sheets and pores (Fig. 3) to determine their size. In general, the pore size decreases with increasing sheet thickness and decreasing porosity. Porous biomaterials with a similar

porosity such as P700, I600, G700, and D600, show different values for the sheet thickness, pore size and surface area (Table 2).

3.2. Permeability values

Sixty-four samples were tested experimentally (four samples of every type of TPMS geometry with four different apparent densities). The measurements were repeated five times for every sample, resulting in twenty measurements for every type of porous biomaterial.

A graph with the pressure drop ΔP as a function of flow velocity v through the sample was used to determine the experimental values for the laminar region (Supplementary document Fig. S1). The permeability values (Fig. 4) were found to be dependent on the apparent density of the porous biomaterials, i.e. the permeability decreases with increasing apparent density. Furthermore, the permeability depended on the geometry of the unit cell, regardless of the apparent density of the specimens (Fig. 4). For example, the I-WP specimens have a lower permeability than the diamond specimens up to an apparent density of 43%. It was found that
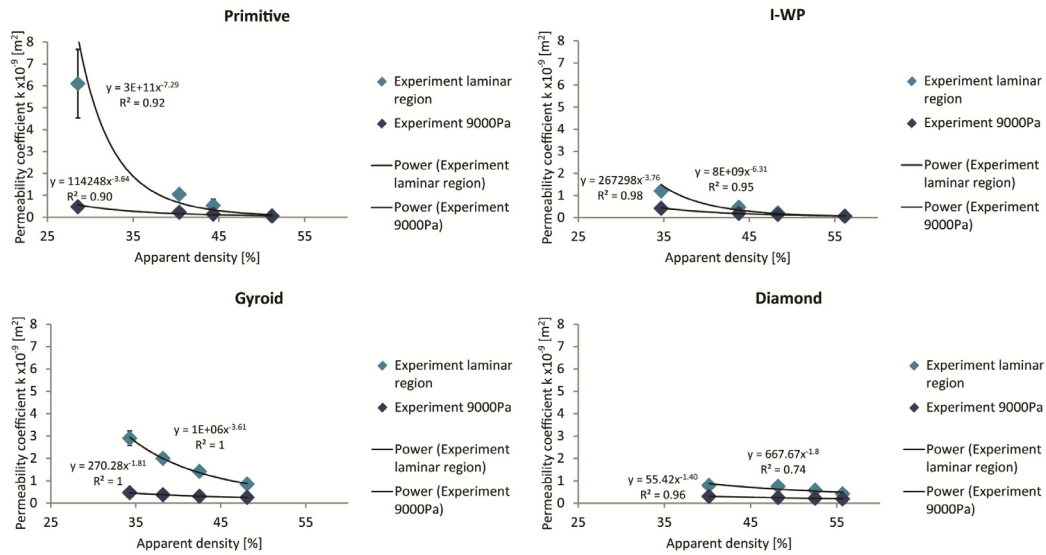
Fig. 4. Permeability values derived from the experiments for the different apparent densities of the TPMS porous biomaterials. Green and blue dots represent the permeability values obtained from the laminar region 1 < Re < 10 and for a pressure gradient of 9000 Pa (turbulent flow).

the permeability decreases with increasing flow velocities due to growing inertial effects (Fig. 4). The highest (6.1×10^{-9} m^2) and lowest (5.5×10^{-11} m^2) permeability values for the laminar regime were found for the P500 and I800 samples, respectively. For a pressure difference of 9000 Pa, the permeability varied between 4.9×10^{-11} m^2 and 4.8×10^{-10} m^2.

3.3. Mechanical tests

3.3.1. Static mechanical tests

Nine samples of every type of porous biomaterial were used for the mechanical tests. Six samples were subjected to static compression with or without lubricant (three for each test) and three to compression-compression fatigue tests. The stress-strain curves obtained from the static compression tests were used to derive different mechanical properties. These include the plateau stress σ_{pl}, quasi-elastic gradient, and yield stress σ_y. The values shown in the following graphs are the averages of the three samples of every type of porous biomaterial used for the tests.

Different failure modes were observed for the different types of porous biomaterials during the static compression tests (Fig. 5 Compression, Supplementary document Table S1). These failure modes are dependent on the geometry of the unit cell and could be related to the stress-strain curves (Fig. 6, Supplementary document Fig. S2). All primitive and gyroid specimens, and I-WP specimens with a low apparent density showed barrelling. In this case, the mid height of the sample was bulging out and layers collapsed onto each other (Fig. 5b). The I-WP with a higher apparent density and all diamond specimens failed due to shear band localization (Fig. 5a, c). One or multiple shear bands (Fig. 5a, c) were observed in these specimens. In the primitive specimens with the highest density, shear bands were visible, but no shear fracture occurred (Fig. 5d Compression).

The stress-strain curves were typical for porous biomaterials [29,30] with the same stages of deformation and same features including the linear increase in stress with strain, a relatively long plateau region with fluctuating stresses, and finally a region of rapid increase in stress (Fig. 6, Supplementary document Fig. S2).

It was observed that the peaks and valleys in the stress-strain curves (Fig. 6, Supplementary document Fig. S2) were caused by the formation of shear lines and the build-up of stresses after the

load was transferred to neighboring sheets or unit cells. The stress-strain curves of the diamond specimens (Fig. 6, Supplementary document Fig. S2) have a short yield plateau, after which the curves demonstrated large levels of irregularity due to shear fracture of the samples.

The stress-strain curves remained largely similar when the samples were tested with or without lubricant (Fig. 6, Supplementary document Fig. S2). Some samples of the D700 and D800 failed under pure shear before 20% strain was reached. Because the plateau stress σ_{pl}, is defined as the mean stress between 20% and 30% strain, these values presented in Supplementary document Fig. S3 are based on only one or two measurements.

For all types of porous biomaterials, the yield stress σ_y, and plateau stress σ_{pl}, increased with increasing apparent density (Fig. 7, Supplementary document Fig. S3). A slightly higher plateau stress was observed for the samples tested with lubricant.

The values of the quasi-elastic gradient of the primitive, I-WP, and gyroid samples tested without lubricant increased almost linearly with increasing apparent density (Fig. 8). For all porous biomaterials, the values for the quasi-elastic gradient were reduced with the application of lubricant.

#### 3.3.2. Fatigue behavior of the porous biomaterials

The primitive specimens showed the shortest fatigue life with a maximum amount of approximately 3×10^4 cycles. The fatigue life of the I-WP, diamond and gyroid specimens varied between 1×10^5 and 7×10^5 cycles. It was observed that the primitive and I-WP specimens show a slight increase in cycles to failure as the apparent density increased, while the opposite held for the gyroid specimens (Fig. 9). Generally, the fatigue samples of all types of unit cells failed under a 45° angle (Fig. 5 LOM). Two types of specimens from the diamond and I-WP structures, namely the D500 and I800, were still intact after 1×10^6 cycles (Fig. 9).

In the primitive and gyroid specimens, crack initiation was observed at the inside of the unit cells (Fig. 5 LOM). The optical microscopy images of the I-WP show crack development at manufacturing imperfections and small pores in the bulk material (Fig. 5 LOM). The weak parts of the geometry seem to be the connections between two unit cells, and the vertical and horizontal sheets. Although no macroscopic damage of the diamond (D500) specimens was observed after 1×10^6 cycles, cracks were present

Compression
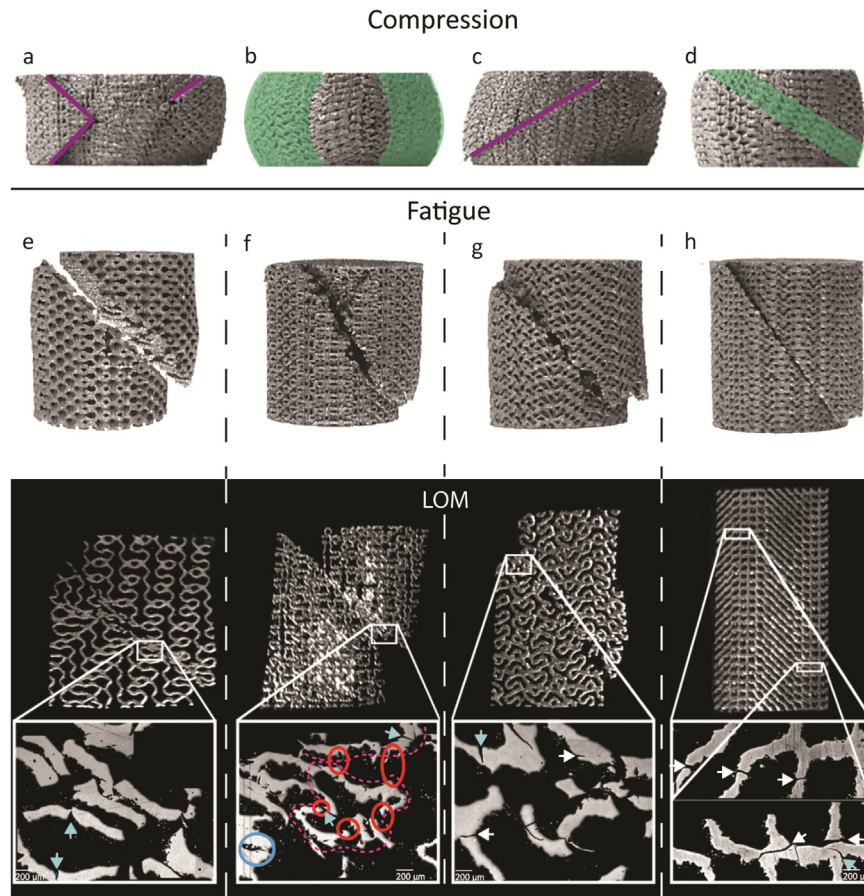
Fatigue

Fig. 5. Compression – Different failure modes of samples during the static compression tests. a. shear lines (purple) in different directions, b. barrelling (green), c. one shear line (purple), d. diagonal collapsing (green) of layers.Fatigue – Shear failure at 45 degrees of specimens after fatigue tests and LOM images of embedded samples. The pink dashed line shows the boundary of one unit cell. The white arrows indicate the initiation of crack formation. The blue arrows indicate crack formation from the inside of the unit cell. The circles in the LOM images of the I-WP specimen (f) indicate examples of crack formation due to manufacturing imperfections (blue) and weak parts of the structure (red). e. primitive, f. I-WP, g. gyroid, h. diamond. (For interpretation of the references to colour in this figure legend, the reader is referred to the web version of this article.)
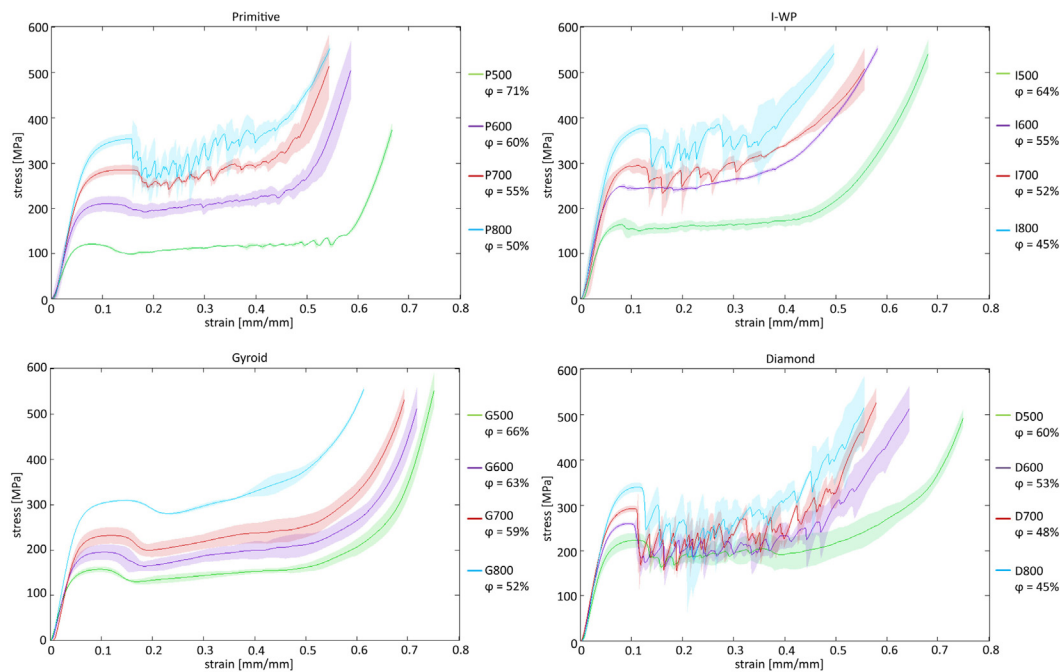
Fig. 6. Stress-strain curves for the primitive, I-WP, gyroid and diamond specimens with four different porosities of the static compression tests performed with a strain rate of 1.2 mm/s. The shadow around the curves represents the standard deviation from the mean of three samples.
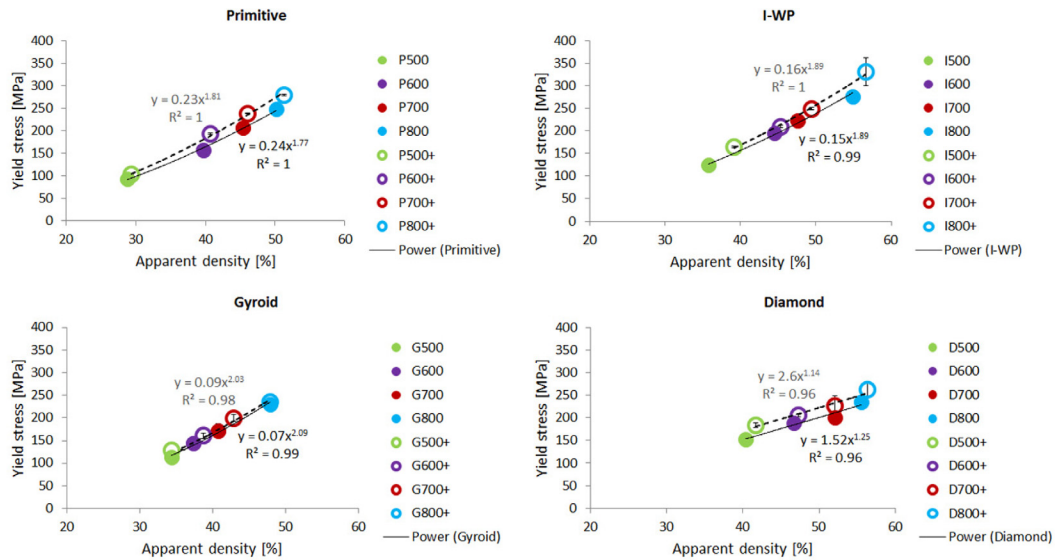
Fig. 7. Yield stress for the different porosities of the primitive, IWP, gyroid and diamond porous biomaterials. The '+' sign indicates the values of the tests with MoS2 lubricant.
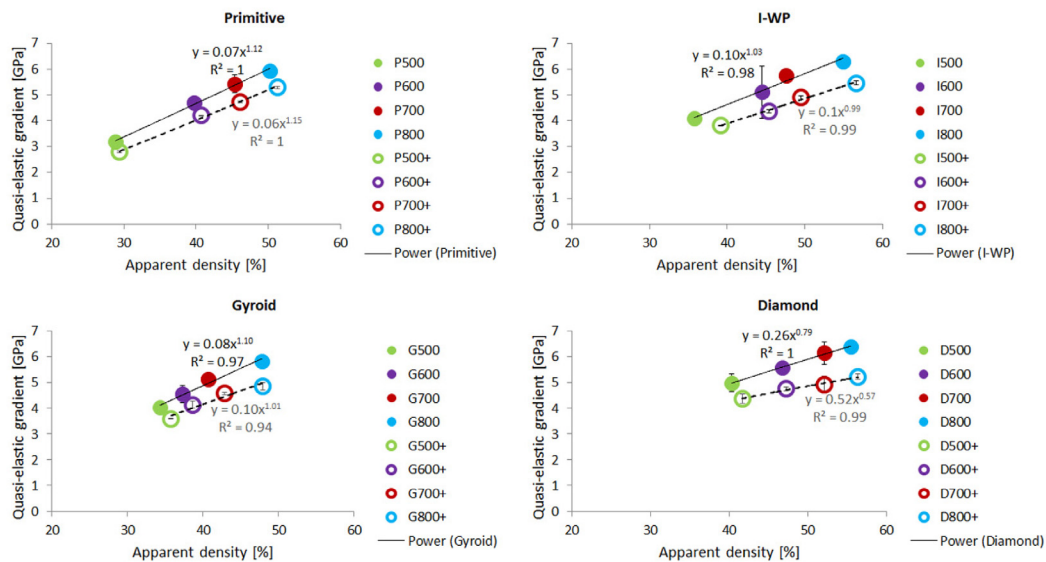
Fig. 8. Quasi-elastic gradient for the different porosities of the primitive, I-WP, gyroid and diamond specimens. The '+' sign indicates the values of the tests with MoS2 lubrication.

within the samples (Fig. 5 Fatigue). These cracks initiated in the sheets at the periphery of the specimen and propagated to the center via the vertical sheets (Fig. 5, LOM). Cracks were also visible in the intersections of the horizontal and vertical sheets (Fig. 5, LOM).

4. Discussion

AM porous metallic biomaterials based on four different types of triply periodic minimal surfaces and with relatively wide range of relevant porosities were developed in the current study. The results of the characterization test introduced earlier show that the developed biomaterials present an interesting combination of morphological properties, quasi-static mechanical behavior, fatigue resistance, and permeability. These properties make them excellent bone-mimicking biomaterials that can withstand fairly large deformations (>0.5%) and exhibit exceptionally high fatigue strength. These results make them potential candidates as bone-mimicking orthopedic implant designs and bone-substituting biomaterials.

4.1. Morphological properties

The morphological properties of the porous structures characterized using micro-CT and dry weighing are very close to their design values. That is an important point given the fact that the specific design morphology of minimal surfaces (i.e. a mean curvature of zero) needs to be preserved after the additive manufacturing process, to make sure the morphology resembles that of trabecular bone. Additive manufacturing of such complex geometrical surfaces at the micro-scale is quite challenging. This is partially caused by the different and continuously changing orientation of the plate-like structures that constitute the micro-architecture of such biomaterials. For example, specific parts of the micro-architecture of some of the minimal surfaces are in parallel with the powder bed while the other regions make a certain
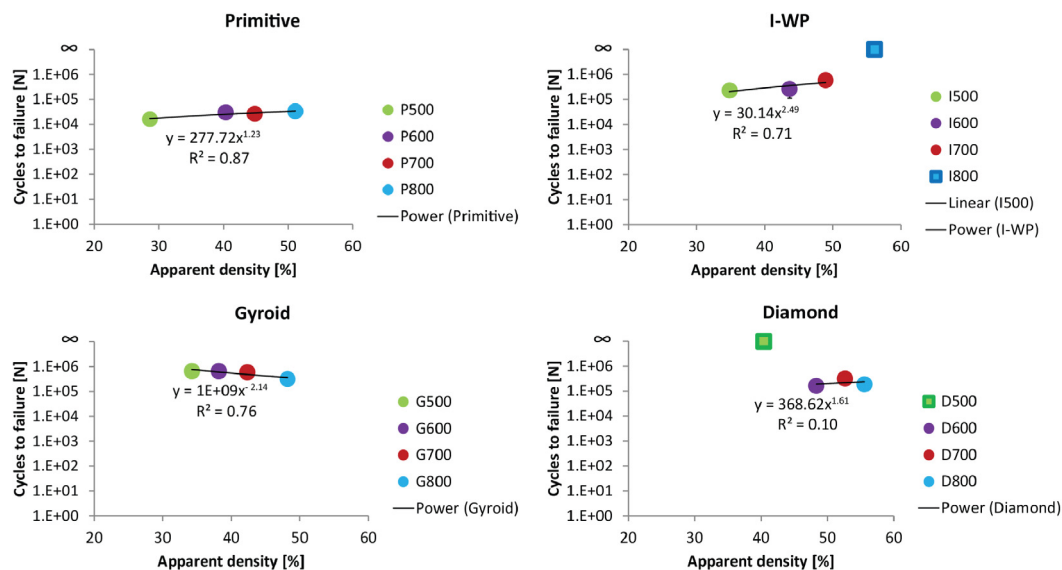
Fig. 9. Number of cycles to failure for the different apparent densities of the primitive, I-WP, gyroid and diamond specimens. The blue and green square markers for the I800 and D500 in the I-WP and diamond figures indicate that these samples were still intact after 10^6 cycles.

Table 3
Comparison between the morphological properties of the AM porous biomaterials presented here and those of trabecular bone from the different regions of the human body.

	TPMS	Various regions [68]	Calcaneus [69]	Femoral head [69]	Iliac crest [69]	Lumbar spine [69]	Femoral neck [70]	Greater trochanter [70]	Vertebrae [70]	Iliac crest [71]
BV/TV	0.29–0.61	0.06–0.36	0.05–0.19	0.08–0.32	0.06–0.28	0.04–0.12	0.25 ± 0.06	0.10 ± 0.02	0.11 ± 0.03	0.20
Tb.Th (µm)	244–444	100–190	102–169	120–257	101–225	82–157	178 ± 27	133 ± 14	141 ± 17	100
Tb.Sp. (µm)	361–896	320–1670	456–982	480–984	523–1306	612–1269	620 ± 82	966 ± 146	922 ± 151	395
DA	0.13–0.36	1.11–2.54	1.36–2.17	1.27–2.18	1.17–1.97	1.16–1.96	–	–	–	–

angle with the powder bed. Proper solidification of the melted powder to yield fully solid (i.e. pore-free) bulk (i.e. matrix) material is particularly difficult for the horizontal parts of micro-architecture [31] due to the disruption of heat transfer by the powder bed. Moreover, the parameters used for the horizontal parts of the micro-architecture may not work for the other parts of the micro-architecture with different orientation. Therefore, the laser processing parameters had to be optimized for every porosity of every type of minimal surface. This was done during an extensive parametric study to make sure the bulk material constituting the porous biomaterial contained the least possible amount of pores.

Specific requirements have been laid out through past research regarding the morphological properties that are required for maximum bone tissue regeneration performance of biomaterials. One important parameter is the pore size whose effect on tissue regeneration performance have been extensively researched. Through extensive review of the past research, Karageorgiou and Kaplan [32] identified a recommended pore size of >300 µm. Micro-CT analysis showed that the actual pore sizes of all AM porous biomaterials developed here are above 300 µm.

When comparing the morphological properties of the AM porous biomaterials developed here and those of the trabecular bone (Table 3), it is clear that trabecular spacing (pore size) is well within the range of the values reported for bone. The BV/TV values found for TPMS also overlaps with the values reported for trabecular bone in a few other studies (Table 3). The trabecular thickness values measured for AM porous biomaterials are somewhat higher than those observed for trabecular bone (Table 3). However, the largest difference is between the degree of anisotropy of the AM porous biomaterials presented here and those reported for trabec-

ular bone in the literature (Tables 2 and 3). The AM porous biomaterials based on TPMS are much more isotropic than the native bone tissue. The effect of this difference on the process of bone tissue regeneration is difficult to predict. Anisotropy in native bone tissue is thought to be related to the need for maximizing stiffness and strength in the main loading direction, while keeping the bone mass as low as possible. The above-mentioned concerns may be less applicable in the case of metallic biomaterials where the strength and stiffness of the bulk material, from which the porous structures are made, are much higher than those of bone tissue.

In addition to surface properties [33–36] and functional groups [37,38] that are known to profoundly affect the bone tissue regeneration process, curvature has been identified recently as a parameter influencing tissue regeneration [8–11,13]. The sign and magnitude of surface curvature are shown to drastically influence the size and rate of tissue regeneration [8–11,13]. An important bone-mimicking aspect of the AM porous biomaterials presented here is the fact that they mimic the curvature characteristics of trabecular bone. The mean curvature of trabecular bone is close to zero [14,15], which is the same as the mean curvature of minimal surfaces. The effects of curvature on tissue regeneration have been explained through the mechanotransduction pathways that involve curvature-induced tensile stresses [9,10,13,39] and might result in the reorganization of the cytoskeleton. There is therefore a mechanistic connection between the potential mechanism through which minimal surfaces could improve bone tissue regeneration performance and the mechanotransduction pathways of curvature-driven tissue regeneration. Indeed, a computational model describing the effects of curvature on tissue regeneration used geometries that could evolve to become minimal surfaces [13].

Table 4
Comparison between the mechanical and physical properties of AM porous biomaterials based on TPMS and those of human bone tissue.

	TPMS	Different regions of the human body/region unknown	Vertebra	Proximal tibia	Greater trochanter	Femoral neck	Femur	Proximal femur
E (MPa)	3200–6400	16–1113 (T) [68] 10–1570 (T) [72] 5000–23,000 (C) [72]	90–536 (T) [73] 100–800 (T)[40]	200–2800 (T) [40] 445±257 (T) [74]	200–1500 (T) [40]	750–4500 (T) [40]	389±270 (T) [75] 16,700 (C) [76]	441±271 (T) [77]
σ_y (MPa)	92–276	164–240 (C) [72]	0.56–3.71 (T)[73]	–	–	55.3±8.6 (T) [40]	122.3 (C) [76]	–
$\kappa \times 10^{-9}$ (m²)	0.05–6.10	–	8.05±4.75 (T) [57]	0.467–14.8 (T) [78]	–	–	–	2.76±1.91 (T) [57]

T: trabecular bone, C: cortical bone.

4.2. Quasi-static mechanical properties

The mechanical behavior of the developed biomaterials in terms of their quasi-static mechanical properties and fatigue resistance were studied. Also the fluid flow properties of the associated porous structures were characterized in terms of permeability. The quasi-elastic gradient of the developed porous biomaterials, which is the closest concept to elastic modulus in the study of the mechanical behavior of porous biomaterials, was found to be between 3.2 and 6.4 GPa. The above-mentioned range largely overlaps with the higher end of the apparent elastic moduli reported for trabecular bone in a study by Morgan et al. [40] (Table 4). They evaluated trabecular bone from different areas in the body with varying apparent densities that showed elastic moduli between 0.1 and 4.5 GPa (Table 4) [40]. The quasi-elastic modulus of the AM porous biomaterials was also close to the lower end of the elastic modulus of cortical bone reported in the literature; e.g. see values reported in Ref. [41] (Table 4). In terms of yield stress, the values measured for the AM porous biomaterials were similar to some values measured for cortical bone [42] and generally higher than those measured for trabecular bone [43] (Table 4). The plateau stress is also generally higher for the biomaterials developed here as compared to the compressive strength values reported for both trabecular and cortical bone [42–44]. The AM porous biomaterials based on triply periodic minimal surfaces therefore show a combination of relatively low elastic moduli which are in the range of those observed for trabecular and cortical bone and relatively high yield stress and compressive strength. This is a desirable combination for bone-substituting biomaterials because the relatively low elastic modulus ensures the minimal chance of stress shielding. Stress shielding occurs when an implant with a higher stiffness carries more load than the bone around the implant. This leads to bone resorption and eventually implant failure [45]. Because the quasi-elastic gradient, i.e. stiffness of the porous biomaterials studied here, is within the range of the stiffness of bone, stress shielding is less likely to occur. At the same time, the relatively high mechanical strength of the bone-substituting biomaterial provides enough mechanical support and prevents the biomaterial to fail under mechanical loading. Given the fact that the elastic modulus and mechanical stress are positively correlated with each other for most naturally occurring materials, it is often impossible to develop biomaterials that show low enough elastic modulus while preserving high mechanical strength. The rationally designed biomaterials presented in the current study, although based on minimal surfaces, could combine both desired features. This is partially due to their sheet-based micro-architectures structure as compared to strut-based (i.e. beam-based) micro-architectures that are used in development of many other types of porous biomaterials. These findings are in line with the previous findings that the ratio of yield strength to elastic modulus is dependent on the micro-architecture of porous biomaterials [46].

It is also important to note that friction could play an important role in determining the quasi-static mechanical properties of AM porous biomaterials. The use of a consistent testing protocol with sufficient lubrication to minimize the friction is therefore recommended, particularly when one is interested the in large deformation behavior of the biomaterials.

4.3. Fatigue behavior

One of the limitations of most AM porous biomaterials developed to date is their relatively low fatigue resistance. In many studies, the endurance limit (the stress level for which the number of number of loading cycles before failure exceeds a certain threshold, e.g. 1×10^6 cycles) of such biomaterials is found to be below $\approx$20% of the plateau (or yield) stress [47,48]. An important

property of the AM porous biomaterials developed in the current study is their extremely high fatigue resistance as compared to comparable AM porous biomaterials developed during the recent years. When loaded at a stress level as high as 60% of their yield stress, the number of cycles to failure is more than the specified threshold (i.e. 1×10^6 cycles) for some of the porous structures developed in the current study (e.g. I800 and D500). Once a specimen has endured more than the specified number of loading cycles, fatigue tests are usually stopped and the specimens are assumed to have indefinite fatigue life for all practical purposes.

With a value as high as 60% of their yield stress as their endurance limit, the maximum endurance limit of these porous structures is at least three times higher than that of AM porous metallic biomaterials developed before. A threshold of 1×10^6 loading cycles is generally used in this kind of studies on AM porous biomaterials that are aimed for application in orthopedic implants. This is because the average patient walking activity is shown to be around 2 million cycles per year (i.e. 52 weeks) [49] and the mean bone fracture healing time is estimated to be ≈16 weeks for otherwise (skeletally) healthy patients [50]. Once bone has grown into the pores of the biomaterial, the fatigue strength of the bone-implant complex increases by up to ≈10 folds even for bone tissue with very low mechanical properties (as might be the case for immature bone) [51].

The much improved level of normalized fatigue resistance in the AM porous biomaterials developed in the current study is likely due to the topology of the internal structure of the biomaterials which is based on sheets rather than beams. Fatigue resistance is related to the crack initiation points, which in the case of AM porous biomaterials are the notches created through the AM process [52,53]. Beam-based designs [31,52–55] are much more prone to development of notches as compared to sheet-based designs such as TPMS. That is partially due to the fact that beam-based designs are often made through sintering of a limited number of powder particles, and the diameter of the struts is usually comparable with the accuracy of the AM technique. In contrast, sheet-based designs such as those based on TPMS have much more smooth and connected geometries that are made from many particles. Therefore, in comparison with beam-based porous structures, continuous sheet-based porous structures are expected to be less sensitive to such imperfections, which could greatly improve their fatigue resistance. Such high levels of fatigue resistance are generally very important for practical application of the developed AM porous biomaterials, because implants could be designed for much higher levels of stress without concerns for patient safety.

4.4. Permeability

The permeability of the AM porous biomaterials developed here are in the range of permeability values reported for trabecular bone in the literature (Table 4) [45,56,57]. Similar to trabecular bone [45,57], the permeability of the biomaterials presented here decreases as the apparent density increases (i.e. porosity values decrease). This is in line with the findings of other studies, which have found that the permeability of porous biomaterials and scaffolds is correlated with their porosity, as long as the pores are interconnected [3]. Increased surface area is expected to decrease permeability due to the additional frictional forces [58]. In the porous biomaterials developed here, the surface area generally increases with porosity. Since we found the permeability to increase with porosity, it can be concluded that the effects of increased porosity on permeability are more pronounced as compared to the effects of any increase in frictional forces that might occur due to the increased surface area.

Cell nutrition and oxygenation are dependent on diffusion before the completion of angiogenesis. The reach and speed of

mass transport taken place through the diffusion process are dependent on the morphology of the porous biomaterials and their permeability. If high values of pressure and/or concentration gradients are required to transfer nutrients and oxygen to the cells residing in the deepest part of the porous biomaterial, there is a high chance that cell metabolism is disrupted at least in some parts of the biomaterial and tissue regeneration does not properly progress. Proper values of permeability are therefore important for ensuring unhindered mass transport within biomaterials to maximize their bone tissue regeneration performance. Even though the absolute values of permeability measured here are found to be dependent on the type of flow conditions, particularly for the primitive and gyroid type of minimal surfaces, the permeability values measured for both types of fluid flow remain within the reported values of permeability of trabecular bone. That is partially due to the relatively large span of permeability values reported for trabecular bone [45,56,57]. In any case, more predictability of permeability values may be beneficial during the rational design process of bone-substituting biomaterials. This predictability would help when a good description of the physical properties of the biomaterials is essential for computational modeling of the bone tissue regeneration process. It is important to realize that permeability values are known to be anisotropic also in trabecular bone [59].

4.5. Design implications

In general, availability of libraries which relate the micro-architecture of porous biomaterials to their physical and mechanical properties such as permeability, elastic modulus, and fatigue life could greatly facilitate the design process [60–63]. We presented a class of AM porous biomaterials based on different types of TPMS and with different dimensions in this study. The results of our study show that these materials are generally capable of mimicking the properties of bone tissue. Application of the specific members of this class of porous biomaterials in the design of orthopedic implants may, however, require additional design considerations. For example, the type of TPMS used in different anatomical locations may need to be different or there might be a need for gradients in terms of porosity and/or TPMS type to better mimic the highly complex and spatially varying structure of trabecular bone. One of the limitations of the current study is that the *in vitro* and *in vivo* experiments required for evaluation of the tissue regeneration performance of the developed biomaterials have not been performed.

Although many studies aiming at development of porous biomaterials try to mimic the properties of bone, it is worth noting that the structure of the bone tissue at its equilibrium state may not necessarily be the best structure for the enhancing the bone tissue regeneration process, which is a transient state and far from equilibrium. Therefore, it may be necessary to simulate the bone regeneration process while considering mechanobiological aspects [64,65] and theoretical models [66]. This could improve the design of the micro-architecture of bone-substituting biomaterials. Such an approach would allow for direct consideration of the local loading conditions experienced by cells residing on the surface of porous biomaterials [67] and, thus a more mechanistic design methodology.

5. Conclusions

Porous metallic biomaterials based on four different types of triply periodic minimal surfaces and with different porosities were rationally designed, additively manufactured, and characterized to evaluate their suitability for orthopedic applications. The combination of topological, mechanical, and physical properties exhib-

ited by these biomaterials suggests they are promising bone-mimicking biomaterials. In terms of topology, the rationally designed micro-architecture of the porous structures resembled the topological properties of trabecular bone including a mean curvature close to zero. Most porous biomaterials have a highly correlated elastic modulus and (yield) strength. However, the biomaterials developed here showed a unique combination of relatively low elastic moduli in the range of those observed for trabecular bone and high yield stress exceeding those reported for cortical bone. With this combination of relatively low elastic moduli and high yield strength, it is possible to simultaneously avoid stress shielding while providing strong mechanical support for bone regeneration and osseointegration. Furthermore, as opposed to other AM porous biomaterials developed to date, the biomaterials developed in the current study also show extremely high fatigue resistance with some of the porous structures showing an endurance limit as high as 60% of their yield stress. This compares to endurance limits in the range of $\approx$20% of plateau/yield stress reported for previously developed AM porous metallic biomaterials. Finally, the permeability values measured for the developed biomaterials were in the range of permeability values reported for trabecular bone in the literature. Based on above-mentioned results, the additionally manufactured porous biomaterials developed here seem to hold significant promise for orthopedic applications. However, *in vivo* studies should be performed to evaluate their actual bone regeneration performance.

Appendix A. Supplementary data

Supplementary data associated with this article can be found, in the online version, at http://dx.doi.org/10.1016/j.actbio.2017.02.024.

References

[1] M. Dias, P. Fernandes, J. Guedes, S. Hollister, Permeability analysis of scaffolds for bone tissue engineering, J. Biomech. 45 (6) (2012) 938–944.
[2] S.J. Hollister, Porous scaffold design for tissue engineering, Nat. Mater. 4 (7) (2005) 518–524.
[3] T.S. Karande, J.L. Ong, C.M. Agrawal, Diffusion in musculoskeletal tissue engineering scaffolds: design issues related to porosity, permeability, architecture, and nutrient mixing, Ann. Biomed. Eng. 32 (12) (2004) 1728–1743.
[4] X. Wang, S. Xu, S. Zhou, W. Xu, M. Leary, P. Choong, M. Qian, M. Brandt, Y.M. Xie, Topological design and additive manufacturing of porous metals for bone scaffolds and orthopaedic implants: a review, Biomaterials 83 (2016) 127–141.
[5] S. Li, Q. Xu, Z. Wang, W. Hou, Y. Hao, R. Yang, L. Murr, Influence of cell shape on mechanical properties of Ti–6Al–4V meshes fabricated by electron beam melting method, Acta Biomater. 10 (10) (2014) 4537–4547.
[6] S. Amin Yavari, L. Loozen, F.L. Paganelli, S. Bakhshandeh, K. Lietaert, J.A. Groot, A.C. Fluit, C.E. Boel, J. Alblas, H.C. Vogely, H. Weinans, A. Zadpoor, Antibacterial behavior of additively manufactured porous titanium with nanotubular surfaces releasing silver ions, ACS Appl. Mater. Interfaces 8 (27) (2016) 17080–17089.
[7] J. van der Stok, M. Koolen, M. de Maat, S.A. Yavari, J. Alblas, P. Patka, J. Verhaar, E. van Lieshout, A.A. Zadpoor, H. Weinans, H. Jahr, Full regeneration of segmental bone defects using porous titanium implants loaded with BMP-2 containing fibrin gels, Eur. Cells Mater. 2015 (29) (2015) 141–154.
[8] A.A. Zadpoor, Bone tissue regeneration: the role of scaffold geometry, Biomater. Sci. 3 (2) (2015) 231–245.
[9] C.M. Bidan, K.P. Kommareddy, M. Rumpler, P. Kollmannsberger, Y.J. Bréchet, P. Fratzl, J.W. Dunlop, How linear tension converts to curvature: geometric control of bone tissue growth, PLoS One 7 (5) (2012) e36336.
[10] C.M. Bidan, K.P. Kommareddy, M. Rumpler, P. Kollmannsberger, P. Fratzl, J.W. Dunlop, Geometry as a factor for tissue growth: towards shape optimization of tissue engineering scaffolds, Adv. Healthcare Mater. 2 (1) (2013) 186–194.
[11] M. Rumpler, A. Woesz, J.W. Dunlop, J.T. van Dongen, P. Fratzl, The effect of geometry on three-dimensional tissue growth, J. R. Soc. Interface 5 (27) (2008) 1173–1180.
[12] H. Karcher, K. Polthier, Construction of triply periodic minimal surfaces, Philos. Trans. R. Soc. London A 354 (1715) (1996) 2077–2104.
[13] C.M. Bidan, F.M. Wang, J.W. Dunlop, A three-dimensional model for tissue deposition on complex surfaces, Comput. Methods Biomech. Biomed. Eng. 16 (10) (2013) 1056–1070.
[14] H. Jinnai, Y. Nishikawa, M. Ito, S.D. Smith, D.A. Agard, R.J. Spontak, Topological similarity of sponge-like bicontinuous morphologies differing in length scale, Adv. Mater. 14 (22) (2002) 1615–1618.
[15] H. Jinnai, H. Watashiba, T. Kajihara, Y. Nishikawa, M. Takahashi, M. Ito, Surface curvatures of trabecular bone microarchitecture, Bone 30 (1) (2002) 191–194.
[16] S.T. Hyde, G.E. Schröder-Turk, Geometry of interfaces: topological complexity in biology and materials, Interface Focus 2 (5) (2012) 529–538.
[17] S.C. Kapfer, S.T. Hyde, K. Mecke, C.H. Arns, G.E. Schröder-Turk, Minimal surface scaffold designs for tissue engineering, Biomaterials 32 (29) (2011) 6875–6882.
[18] J.W. Galusha, L.R. Richey, J.S. Gardner, J.N. Cha, M.H. Bartl, Discovery of a diamond-based photonic crystal structure in beetle scales, Phys. Rev. E 77 (5) (2008) 050904.
[19] J.W. Galusha, L.R. Richey, M.R. Jorgensen, J.S. Gardner, M.H. Bartl, Study of natural photonic crystals in beetle scales and their conversion into inorganic structures via a sol–gel bio-templating route, J. Mater. Chem. 20 (7) (2010) 1277–1284.
[20] S. Hyde, S. Andersson, K. Larsson, Z. Blum, T. Landh, S. Lidin, B. Ninham, The Language of Shape: The Role of Curvature in Condensed Matter: Physics, Chemistry and Biology, Elsevier, 1997.
[21] H.-U. Nissen, Crystal orientation and plate structure in echinoid skeletal units, Science 166 (3909) (1969) 1150–1152.
[22] G. Schröder-Turk, S. Wickham, H. Averdunk, F. Brink, J.F. Gerald, L. Poladian, M. Large, S. Hyde, The chiral structure of porous chitin within the wing-scales of Callophrys rubi, J. Struct. Biol. 174 (2) (2011) 290–295.
[23] V. ABAQUS, 6.13, Dassault Systemes, 2013.
[24] J. Schindelin, I. Arganda-Carreras, E. Frise, V. Kaynig, M. Longair, T. Pietzsch, S. Preibisch, C. Rueden, S. Saalfeld, B. Schmid, Fiji: an open-source platform for biological-image analysis, Nat. Methods 9 (7) (2012) 676–682.
[25] M. Doube, M.M. Kłosowski, I. Arganda-Carreras, F.P. Cordelières, R.P. Dougherty, J.S. Jackson, B. Schmid, J.R. Hutchinson, S.J. Shefelbine, BoneJ: free and extensible bone image analysis in ImageJ, Bone 47 (6) (2010) 1076–1079.
[26] W. Sobieski, A. Trykozko, Darcy's and Forchheimer's laws in practice–Part 1: The experiment, Tech. Sci. 17 (4) (2014) 321–335.
[27] International Organization for Standardization (ISO), ISO 13314: Mechanical Testing of Metals – Ductility Testing – Compression Test for Porous and Cellular Metals, First edition 2011-12-15, 2011.
[28] International Organization for Standardization (ISO), ISO 12108: Metallic Materials – Fatigue Testing – Fatigue Crack Growth Method, Second edition 2012-08-15, 2012.
[29] S. Ahmadi, G. Campoli, S.A. Yavari, B. Sajadi, R. Wauthlé, J. Schrooten, H. Weinans, A. Zadpoor, Mechanical behavior of regular open-cell porous biomaterials made of diamond lattice unit cells, J. Mech. Behav. Biomed. Mater. 34 (2014) 106–115.
[30] S.M. Ahmadi, S.A. Yavari, R. Wauthle, B. Pouran, J. Schrooten, H. Weinans, A.A. Zadpoor, Additively manufactured open-cell porous biomaterials made from six different space-filling unit cells: the mechanical and morphological properties, Materials 8 (4) (2015) 1871–1896.
[31] R. Wauthle, B. Vrancken, B. Beynaerts, K. Jorissen, J. Schrooten, J.-P. Kruth, J. Van Humbeeck, Effects of build orientation and heat treatment on the microstructure and mechanical properties of selective laser melted Ti6Al4V lattice structures, Addit. Manuf. 5 (2015) 77–84.
[32] V. Karageorgiou, D. Kaplan, Porosity of 3D biomaterial scaffolds and osteogenesis, Biomaterials 26 (27) (2005) 5474–5491.
[33] S. Amin Yavari, R. Wauthlé, A.J. Böttger, J. Schrooten, H. Weinans, A.A. Zadpoor, Crystal structure and nanotopographical features on the surface of heat-treated and anodized porous titanium biomaterials produced using selective laser melting, Appl. Surf. Sci. 290 (2014) 287–294.
[34] A.B. Faia-Torres, S. Guimond-Lischer, M. Rottmar, M. Charnley, T. Goren, K. Maniura-Weber, N.D. Spencer, R.L. Reis, M. Textor, N.M. Neves, Differential regulation of osteogenic differentiation of stem cells on surface roughness gradients, Biomaterials 35 (33) (2014) 9023–9032.
[35] R.A. Gittens, T. McLachlan, R. Olivares-Navarrete, Y. Cai, S. Berner, R. Tannenbaum, Z. Schwartz, K.H. Sandhage, B.D. Boyan, The effects of combined micron-/submicron-scale surface roughness and nanoscale features on cell proliferation and differentiation, Biomaterials 32 (13) (2011) 3395–3403.
[36] Y. Khan, M.J. Yaszemski, A.G. Mikos, C.T. Laurencin, Tissue engineering of bone: material and matrix considerations, J. Bone Joint Surg. 90 (Supplement 1) (2008) 36–42.
[37] X. Li, J. Lan, M. Ai, Y. Guo, Q. Cai, X. Yang, Biomineralization on polymer-coated multi-walled carbon nanotubes with different surface functional groups, Colloids Surf. B 123 (2014) 753–761.
[38] S. Zhao, J. Zhang, M. Zhu, Y. Zhang, Z. Liu, Y. Ma, Y. Zhu, C. Zhang, Effects of functional groups on the structure, physicochemical and biological properties of mesoporous bioactive glass scaffolds, J. Mater. Chem. B 3 (8) (2015) 1612–1623.
[39] E. Gamsjäger, C. Bidan, F. Fischer, P. Fratzl, J. Dunlop, Modelling the role of surface stress on the kinetics of tissue growth in confined geometries, Acta Biomater. 9 (3) (2013) 5531–5543.
[40] E.F. Morgan, H.H. Bayraktar, T.M. Keaveny, Trabecular bone modulus–density relationships depend on anatomic site, J. Biomech. 36 (7) (2003) 897–904.
[41] K. Choi, J. Kuhn, M. Ciarelli, S. Goldstein, The elastic moduli of human subchondral, trabecular, and cortical bone tissue and the size-dependency of cortical bone modulus, J. Biomech. 23 (11) (1990) 1103–1113.

[42] D.T. Reilly, A.H. Burstein, The elastic and ultimate properties of compact bone tissue, J. Biomech. 8 (6) (1975). 393IN9397–396IN11405.
[43] J.W. Vahey, J.L. Lewis, R. Vanderby, Elastic moduli, yield stress, and ultimate stress of cancellous bone in the canine proximal femur, J. Biomech. 20 (1) (1987) 29–33.
[44] L.J. Gibson, The mechanical behaviour of cancellous bone, J. Biomech. 18 (5) (1985) 317–328.
[45] D.A. Shimko, V.F. Shimko, E.A. Sander, K.F. Dickson, E.A. Nauman, Effect of porosity on the fluid flow characteristics and mechanical properties of tantalum scaffolds, J. Biomed. Mater. Res. B Appl. Biomater. 73 (2) (2005) 315–324.
[46] M. Wettergreen, The Effect of Material Organization on the Structural Properties of Porous Architectures, Rice University, Department of Bioengineering, 2008.
[47] S. Amin Yavari, S. Ahmadi, R. Wauthle, B. Pouran, J. Schrooten, H. Weinans, A. Zadpoor, Relationship between unit cell type and porosity and the fatigue behavior of selective laser melted meta-biomaterials, J. Mech. Behav. Biomed. Mater. 43 (2015) 91–100.
[48] S. Amin Yavari, R. Wauthlé, J. van der Stok, A. Riemslag, M. Janssen, M. Mulier, J.-P. Kruth, J. Schrooten, H. Weinans, A.A. Zadpoor, Fatigue behavior of porous biomaterials manufactured using selective laser melting, Mater. Sci. Eng. C 33 (8) (2013) 4849–4858.
[49] M. Silva, E.F. Shepherd, W.O. Jackson, F.J. Dorey, T.P. Schmalzried, Average patient walking activity approaches 2 million cycles per year: pedometers under-record walking activity, J. Arthroplasty 17 (6) (2002) 693–697.
[50] V.S. Nikolaou, N. Efstathopoulos, G. Kontakis, N.K. Kanakaris, P.V. Giannoudis, The influence of osteoporosis in femoral fracture healing time, Injury 40 (6) (2009) 663–668.
[51] R. Hedayati, S. Janbaz, M. Sadighi, M. Mohammadi-Aghdam, A. Zadpoor, How does tissue regeneration influence the mechanical behavior of additively manufactured porous biomaterials?, J Mech. Behav. Biomed. Mater. 65 (2017) 831–841.
[52] S. Amin Yavari, S. Ahmadi, J. van der Stok, R. Wauthlé, A. Riemslag, M. Janssen, J. Schrooten, H. Weinans, A.A. Zadpoor, Effects of bio-functionalizing surface treatments on the mechanical behavior of open porous titanium biomaterials, J. Mech. Behav. Biomed. Mater. 36 (2014) 109–119.
[53] J. De Krijger, C. Rans, B. Van Hooreweder, K. Lietaert, B. Pouran, A.A. Zadpoor, Effects of applied stress ratio on the fatigue behavior of additively manufactured porous biomaterials under compressive loading, J. Mech. Behav. Biomed. Mater. (2016). in press.
[54] R. Wauthle, S.M. Ahmadi, S.A. Yavari, M. Mulier, A.A. Zadpoor, H. Weinans, J. Van Humbeeck, J.-P. Kruth, J. Schrooten, Revival of pure titanium for dynamically loaded porous implants using additive manufacturing, Mater. Sci. Eng. C 54 (2015) 94–100.
[55] R. Wauthle, J. Van der Stok, S.A. Yavari, J. Van Humbeeck, J.-P. Kruth, A.A. Zadpoor, H. Weinans, M. Mulier, J. Schrooten, Additively manufactured porous tantalum implants, Acta Biomater. 14 (2015) 217–225.
[56] M.J. Grimm, J.L. Williams, Measurements of permeability in human calcaneal trabecular bone, J. Biomech. 30 (7) (1997) 743–745.
[57] E.A. Nauman, K. Fong, T. Keaveny, Dependence of intertrabecular permeability on flow direction and anatomic site, Ann. Biomed. Eng. 27 (4) (1999) 517–524.
[58] F.J. O'Brien, B.A. Harley, M.A. Waller, I.V. Yannas, L.J. Gibson, P.J. Prendergast, The effect of pore size on permeability and cell attachment in collagen scaffolds for tissue engineering, Technol. Health Care 15 (1) (2007) 3–17.
[59] G. Baroud, R. Falk, M. Crookshank, S. Sponagel, T. Steffen, Experimental and theoretical investigation of directional permeability of human vertebral cancellous bone for cement infiltration, J. Biomech. 37 (2) (2004) 189–196.
[60] B. Bucklen, W. Wettergreen, E. Yuksel, M. Liebschner, Bone-derived CAD library for assembly of scaffolds in computer-aided tissue engineering, Virtual Phys. Prototyping 3 (1) (2008) 13–23.
[61] A.M. Tarawneh, M. Wettergreen, M.A. Liebschner, Computer-aided tissue engineering: benefiting from the control over scaffold micro-architecture, Comp. Aided Tissue Eng. (2012) 1–25.
[62] M. Wettergreen, B. Bucklen, M. Liebschner, W. Sun, CAD Assembly Process for Bone Replacement Scaffolds in Computer-Aided Tissue Engineering, Virtual Prototyping & Bio Manufacturing in Medical Applications, Springer, 2008, pp. 87–111.
[63] M. Wettergreen, B. Bucklen, B. Starly, E. Yuksel, W. Sun, M. Liebschner, Creation of a unit block library of architectures for use in assembled scaffold engineering, Comput. Aided Des. 37 (11) (2005) 1141–1149.
[64] M. Liebschner, B. Bucklen, M. Wettergreen, Mechanical aspects of tissue engineering, in: Seminars in Plastic Surgery, Copyright© 2005 by Thieme Medical Publishers, Inc., 333 Seventh Avenue, New York, NY 10001, USA, 2005, pp. 217–228.
[65] M. Liebschner, M. Wettergreen, Optimization of bone scaffold engineering for load bearing applications, Top. Tissue Eng. (2003) 1–39.
[66] A.A. Zadpoor, Open forward and inverse problems in theoretical modeling of bone tissue adaptation, J. Mech. Behav. Biomed. Mater. 27 (2013) 249–261.
[67] B. Bucklen, Investigation of Surface Mechanical Environment as an Optimization Criterion for Improved Tissue Engineering Scaffolds, Rice University, Department of Bioengineering, 2008.
[68] R. Goulet, S. Goldstein, M. Ciarelli, J. Kuhn, M. Brown, L. Feldkamp, The relationship between the structural and orthogonal compressive properties of trabecular bone, J. Biomech. 27 (4) (1994) 375–389.
[69] D. Ulrich, B. Van Rietbergen, A. Laib, P. Ruegsegger, The ability of three-dimensional structural indices to reflect mechanical aspects of trabecular bone, Bone 25 (1) (1999) 55–60.
[70] G. Bevill, T.M. Keaveny, Trabecular bone strength predictions using finite element analysis of micro-scale images at limited spatial resolution, Bone 44 (4) (2009) 579–584.
[71] P. Rüegsegger, B. Koller, R. Müller, A microtomographic system for the nondestructive evaluation of bone architecture, Calcif. Tissue Int. 58 (1) (1996) 24–29.
[72] X.-N. Gu, Y.-F. Zheng, A review on magnesium alloys as biodegradable materials, Front. Mater. Sci. Chin. 4 (2) (2010) 111–115.
[73] D.L. Kopperdahl, T.M. Keaveny, Yield strain behavior of trabecular bone, J. Biomech. 31 (7) (1998) 601–608.
[74] F. Linde, I. Hvid, B. Pongsoipetch, Energy absorptive properties of human trabecular bone specimens during axial compression, J. Orthop. Res. 7 (3) (1989) 432–439.
[75] A. Rohlmann, H. Zilch, G. Bergmann, R. Kolbel, Material properties of femoral cancellous bone in axial loading, Arch. Orthop. Trauma. Surg. 97 (2) (1980) 95–102.
[76] J.D. Currey, Tensile yield in compact bone is determined by strain, post-yield behaviour by mineral content, J. Biomech. 37 (4) (2004) 549–556.
[77] J.C. Lotz, T.N. Gerhart, W.C. Hayes, Mechanical properties of trabecular bone from the proximal femur: a quantitative CT study, J. Comput. Assist. Tomogr. 14 (1) (1990) 107–114.
[78] A.J. Beaudoin, W.M. Mihalko, W.R. Krause, Finite element modelling of polymethylmethacrylate flow through cancellous bone, J. Biomech. 24 (2) (1991) 127131–129136.